Rotation, spectral variability, magnetic geometry and magnetosphere of the Of?p star CPD −28° 2561[⋆]

G. A. Wade,[1]† R. H. Barbá,[2] J. Grunhut,[3] F. Martins,[4] V. Petit,[5]‡ J. O. Sundqvist,[6] R. H. D. Townsend,[7] N. R. Walborn,[8] E. Alecian,[9] E. J. Alfaro,[10] J. Maíz Apellániz,[10]§ J. I. Arias,[2] R. Gamen,[11] N. Morrell,[12] Y. Nazé,[13,14]¶ A. Sota,[10] A. ud-Doula[15] and the MiMeS Collaboration

Affiliations are listed at the end of the paper

ABSTRACT

We report magnetic and spectroscopic observations and modelling of the Of?p star CPD −28° 2561. Using more than 75 new spectra, we have measured the equivalent width variations and examined the dynamic spectra of photospheric and wind-sensitive spectral lines. A period search results in an unambiguous 73.41 d variability period. High-resolution spectropolari-metric data analysed using least-squares deconvolution yield a Zeeman signature detected in the mean Stokes V profile corresponding to phase 0.5 of the spectral ephemeris. Interpreting the 73.41 d period as the stellar rotational period, we have phased the equivalent widths and inferred longitudinal field measurements. The phased magnetic data exhibit a weak sinusoidal variation, with maximum of about 565 G at phase 0.5, and a minimum of about −335 G at phase 0.0, with extrema approximately in phase with the (double-wave) Hα equivalent width variation. Modelling of the Hα equivalent width variation assuming a quasi-3D mag-netospheric model produces a unique solution for the ambiguous couplet of inclination and magnetic obliquity angles: (i, β) or $(\beta, i) = (35°, 90°)$. Adopting either geometry, the lon-gitudinal field variation yields a dipole polar intensity $B_d = 2.6 \pm 0.9$ kG, consistent with that obtained from direct modelling of the Stokes V profiles. We derive a wind magnetic con-finement parameter $\eta_* \simeq 100$, leading to an Alfvén radius $R_A \simeq 3$–$5R_*$, and a Kepler radius $R_K \simeq 20R_*$. This supports a physical scenario in which the Hα emission and other line variabil-ity have their origin in an oblique, corotating 'dynamical magnetosphere' structure resulting from a magnetically channelled wind. Nevertheless, the details of the formation of spectral lines and their variability within this framework remain generally poorly understood.

Key words: stars: individual: CPD −28° 2561 – stars: magnetic field – stars: massive – stars: rotation.

1 INTRODUCTION

The Of?p stars are mid-O-type stars identified by a number of pecu-liar observational properties. The classification was first introduced by Walborn ([1972]) according to the presence of C III λ4650 emis-sion with a strength comparable to the neighbouring N III lines. Well-studied Of?p stars are now known to exhibit recurrent, and apparently periodic, spectral variations (in Balmer, He I, C III and Si III lines), narrow P Cygni or emission components in the Balmer lines and He I lines, and UV wind lines weaker than those of typical Of supergiants (see Nazé et al. [2010], and references therein).

Only five Galactic Of?p stars are known (Walborn et al. [2010]): HD 108, HD 148937, HD 191612, NGC 1624−2 and CPD −28° 2561. Four of these stars – HD 108, HD 148937, HD 191612 and NGC 1624−2 – have been studied in detail based on optical spectra, and in some cases UV spectra as well. In recent years, they have been carefully examined for the presence of magnetic fields (Donati et al. [2006]; Martins et al. [2010]; Wade et al. [2011], [2012a,b]) and all have

been clearly detected. It therefore appears that the particular spectral peculiarities that define the Of?p classification are a consequence of their magnetism. Indeed, Hubrig et al. (2011, 2012) reported four FORS+VLT measurements of the longitudinal magnetic field of CPD −28° 2561 at the few hundred G level, several of which correspond to detections at somewhat more than 3σ significance.

Like HD 108, HD 191612, HD 148937 and NGC 1624−2, CPD −28° 2561 is a spectroscopic variable star (e.g. Walborn et al. 2010). The spectrum of CPD −28° 2561 was first described as a peculiar Of type by Walborn (1973) and Garrison, Hiltner & Schild (1977). Garrison et al. commented: 'Very peculiar spectrum. Carbon (C III λ4070) is strong, nitrogen weak. H and He II lines are broad, while He I lines are sharp', Walborn classified the spectrum as O6.5fp. The outstanding peculiarity was that although He II λ4686 emission was very strong, appropriate for an Of supergiant, the N III λ4640 emission was incompatibly not.

While Walborn (1973) announced HD 191612 as a new, third member of the Of?p class, it is significant that no such association was made for CPD −28° 2561. The reason was that no C III λ4650 emission was detected in CPD −28° 2561, while a comparable emission strength to that of N III was the primary defining Of?p characteristic. (Of course, it was subsequently discovered that the C III emission disappears entirely at the minimum phase of HD 191612; Walborn et al. 2004; Howarth et al. 2007; Wade et al. 2011.) It was not until the intensive O- and WN-type Stars (OWN) survey's high-resolution monitoring of CPD −28° 2561 (Barbá et al. 2010) revealed extreme variations in λ4686 and Balmer lines, analogous to those of HD 191612, that the association was made (Walborn et al. 2010) and CPD −28° 2561 identified as an Of?p star.

In this paper, we perform a first detailed investigation of the combined magnetic and variability properties of CPD −28° 2561 using an extensive spectroscopic and high-resolution spectropolarimetric data set. In Section 2, we discuss the data acquired and the methods of analysis used. In Section 3, we re-examine the physical properties of the star, as well as its projected rotational velocity. In Section 4, we examine the spectral characteristics and variability, identifying periodic variability of the Hα and other emission and absorption lines and deriving the rotational period of the star. In Section 5, we analyse in detail the magnetic data acquired at the Canada–France–Hawaii Telescope (CFHT). In Section 6, we employ the Hα equivalent width (EW) variation and CFHT magnetic data to constrain the stellar and magnetic geometry and the surface field strength. In Section 7, we derive the magnetospheric properties of CPD −28° 2561. Finally, in Section 8, we summarize our results, and explore the implications of our study, particularly regarding the variability and other properties of CPD −28° 2561, the confinement and structure of its stellar wind, and of the properties of the general class of Of?p stars.

2 OBSERVATIONS

2.1 Spectroscopic observations

Spectroscopic observations of CPD −28° 2561 were obtained in the framework of two spectroscopic surveys: the high-resolution spectroscopic monitoring of southern O- and WN-type Stars (the 'OWN survey'; Barbá et al. 2010) and the Galactic O Star Spectroscopic Survey ('GOSSS'; Maíz Apellániz et al. 2011) In the OWN survey programme, high-resolution and high signal-to-noise ratio (SNR) spectra are being acquired for a sample of 240 massive southern stars selected from the Galactic O Star Catalogue (GOSC version 1; Maíz-Apellániz et al. 2004). One of the goals is to determine

Table 1. Spectrographs used for the acquisition of CPD −28° 2561 spectroscopy and spectropolarimetry.

Spectrograph	Telescope	Spectral range (Å)	Resolving power
Echelle	2.5 m LCO/du Pont	3600–9200	46 000
FEROS	2.2 m ESO/MPI	3500–9200	48 000
REOSC	2.15 m CASLEO	3800–6000	15 000
Boller and Chivens	2.5 m LCO/du Pont	3900–5500	2500
ESPaDOnS	3.6 m CFHT	3650–10000	65 000

precise radial velocities in order to detect new binaries among these stars for which there is scarce or no indication of multiplicity. An additional goal is to detect possible spectral variations which can be related to multiplicity, the presence of magnetic fields, pulsation, or eruptive behaviour. CPD −28° 2561 was included early in the observed sample, and monitored systematically as large variations in the intensity of the He II λ4686 emission line were detected. The star was observed spectroscopically from three different locations: Las Campanas Observatory (LCO), and La Silla Observatory, both in Chile, and Complejo Astronómico El Leoncito (CASLEO), in Argentina, during 33 nights between 2006 and 2012.

Seven spectrograms were obtained with an echelle spectrograph attached to the 2.5 m LCO/du Pont telescope. The spectral resolving power is about 46 000. 12 spectrograms were obtained with the FEROS echelle spectrograph attached to the 2.2 m ESO/MPI telescope. In this case, the spectral resolving power is about 48 000. Additionally, four spectrograms were obtained with the REOSC echelle spectrograph[1] attached to the 2.15 m CASLEO/Jorge Sahade telescope, with a resolving power of about 15 000. Thorium–argon comparison lamp exposures were obtained before or after the science exposures. LCO and CASLEO echelle spectrograms were reduced using the ECHELLE package layered in IRAF,[2] while FEROS spectrograms were reduced using the standard MIDAS pipeline. All spectrograms were bias subtracted, flat-fielded, echelle order identified, and extracted, and finally wavelength calibrated. Table 1 presents technical details of the different spectrographs utilized.

Under the GOSSS programme, we have obtained 10 spectrograms of CPD −28° 2561 between 2008 and 2013 using the Boller and Chivens (B&C) spectrograph attached to the 2.5 m LCO/du Pont telescope, with a spectral resolving power of about 2500. Helium–neon–argon comparison lamps were used for wavelength calibration. A dedicated pipeline was developed for the complete reduction of GOSSS observations. Detailed description about the observing procedures and data reduction is described by Sota et al. (2011) and Sota et al. (2014).

The log of spectroscopic observations is reported in Table 2.

2.2 Spectropolarimetric observations

Spectropolarimetric observations of CPD −28° 2561 were obtained using the ESPaDOnS spectropolarimeter at the CFHT in 2012 and 2013 within the context of the Magnetism in Massive Stars (MiMeS) Large Programme (Wade et al. 2014; Wade et al., in preparation). Altogether, 44 Stokes V sequences were obtained.

---

[1] Jointly built by REOSC and Liège Observatory, and on long-term loan from the latter.

[2] IRAF is the Image Reduction and Analysis Facility, a general purpose software system for the reduction and analysis of astronomical data. IRAF is written and supported by the National Optical Astronomy Observatories (NOAO) in Tucson, Arizona. See iraf.noao.edu.

Table 2. log of spectroscopic observations showing heliocentric Julian Date, rotational phase according to equation (1), and exposure time. The column 'Spectrograph' corresponds to the facilities described in Table 1.

HJD	Phase	Exp. time (s)	Spectrograph
2453875.483	0.511	600	Echelle
2454246.515	0.565	1800	FEROS
2454610.486	0.523	900	B&C
2454627.467	0.754	1800	FEROS
2454786.865	0.926	900	Echelle
2454842.716	0.687	1800	REOSC
2454846.677	0.741	1800	REOSC
2454847.609	0.753	2000	REOSC
2454848.650	0.767	1800	REOSC
2454954.537	0.210	1800	FEROS
2454955.500	0.223	1800	FEROS
2454964.476	0.345	1500	Echelle
2455341.455	0.481	1200	Echelle
2455495.865	0.584	900	B&C
2455604.796	0.068	1800	REOSC
2455641.586	0.569	1800	REOSC
2455643.569	0.596	1800	REOSC
2455646.597	0.637	900	B&C
2455669.553	0.950	900	B&C
2455672.532	0.990	1200	Echelle
2455696.473	0.317	2700	REOSC
2455697.494	0.331	2400	REOSC
2455698.518	0.344	2400	REOSC
2455699.508	0.358	2400	REOSC
2455716.479	0.589	900	B&C
2455898.729	0.072	900	B&C
2455976.599	0.133	1200	Echelle
2456053.500	0.180	900	B&C
2456080.469	0.547	1800	Echelle
2456098.461	0.793	2000	FEROS
2456340.705	0.092	900	B&C
2456367.653	0.460	900	B&C
2456381.587	0.649	900	B&C

Each polarimetric sequence consisted of four individual subexposures taken in different polarimeter configurations. From each set of four subexposures, we derive a mean Stokes V spectrum following the procedure of Donati et al. (1997), ensuring in particular that all spurious signatures are suppressed at first order. Diagnostic null polarization spectra (labelled N) are calculated by combining the four subexposures in such a way that polarization cancels out, allowing us to check that no spurious signals are present in the data (see Donati et al. (1997) for more details on how N is defined). All frames were processed using the Upena pipeline feeding LIBRE-ESPRIT (Donati et al. 1997), a fully automatic reduction package installed at CFHT for optimal extraction of ESPaDOnS spectra. The peak SNR per 1.8 km s^{-1} velocity bin in the reduced spectra range from about 70 to nearly 266, with a median of 200, depending on the exposure time and on weather conditions.

The log of CFHT observations is presented in Table 3.

We also obtained one observation of CPD −28° 2561 with the HARPS instrument in polarimetric model. The observing procedure was fundamentally the same as that described above for ESPaDOnS. Two consecutive observations were acquired with exposure times of 3600 s apiece. The peak SNR of the combined spectrum was 110 per 1 km s^{-1} spectral pixel. The mean HJD of the observation is 2455905.798, corresponding to phase 0.168 according to the ephemeris defined in equation (1).

3 STELLAR PHYSICAL AND WIND PROPERTIES

We have used the atmosphere code CMFGEN (Hillier & Miller 1998) to determine the stellar parameters of CPD −28° 2561. CMFGEN computes non-local thermodynamic equilibrium (NLTE), spherical models including an outflowing wind and line-blanketing. A complete description of the code is given by Hillier & Miller (1998). We have included the following elements in our models: H, He, C, N, O, Ne, Mg, Si, S, Ar, Ca, Fe and Ni. A solar metallicity (Grevesse et al. 2010) was adopted.

We used the classical helium ionization balance method to constrain the effective temperature. As shown in Section 4, spectral variability is observed in He I lines. Part of the variability may be due to emission from the stellar wind (i.e. the magnetosphere inferred later in the paper), contaminating the underlying photospheric features. The determination of T_{eff} is thus difficult. It was performed using spectra #1051146/50 (corresponding to phase 0.718 of the rotational ephemeris described in Section 4) where the He I lines were the strongest, presumably minimizing contamination from the wind and leaving access to the cleanest photospheric profiles. Nevertheless, some wind-sensitive lines are poorly reproduced. Notably He II λ4686 exhibits a P Cyg-like profile, with a strong redshifted absorption that (unlike most other absorption features in the spectrum) is underfitted by the model. The profile of this line may be suggestive of accretion.

The relative strength of He I and He II lines indicates a temperature of about 35 000 K, with an uncertainty of 2000 K. The surface gravity was determined from the wings of the numerous Balmer lines available in the ESPaDOnS spectrum. The line cores are variable but are not the main gravity diagnostics so that our log g estimate is safe. We found that log $g = 4.0 \pm 0.1$ provided the best fit. In absence of strong constraint on the distance of CPD −28° 2561, we decided to adopt a luminosity of $10^{5.35\pm0.15}$ L$_\odot$. This value is intermediate between that of an O6.5 dwarf and giant (Martins, Schaerer & Hillier 2005), and similar to that of the Of?p star HD 191612 (Howarth et al. 2007). The corresponding radius is thus 12.9 ± 3 R$_\odot$. The best fit of the spectrum with maximum He I λ4471 absorption is shown in Fig. 1.

The evolutionary mass, determined from the position in the HR diagram and interpolation between the tracks of Meynet & Maeder (2005), is 35 ± 6 M$_\odot$. The spectroscopic mass, obtained from the surface gravity and the radius, is 61 ± 33 M$_\odot$. The mass estimates are consistent within the error bars, which remain large because of the uncertainties on the distance (and thus on the luminosity). We also note that the evolutionary tracks adopted here do not include the effects of a strong, large-scale stellar magnetic field.

The shape of the photospheric lines could be reproduced with different combinations of rotational velocities and macroturbulence. In the extreme cases, a macroturbulent isotropic velocity of 40 km s^{-1} and a negligible rotational velocity, or no macroturbulence and $v\sin i = 80$ km s^{-1}, correctly reproduce the shape of the photospheric lines. Using C III and N III lines as indicators (C III λ4070 and N III λλ4505–4515 being the main diagnostics), we estimated the nitrogen and carbon content to be N/H $< 5.0 \times 10^{-5}$ and C/H=$(5.0 \pm 3.0) \times 10^{-5}$. Both elements are underabundant compared to the Sun, which seems consistent with the location of the

Table 3. log of ESPaDOnS spectropolarimetric observations. Columns indicate CFHT archive unique identifier, heliocentric Julian Date, exposure duration, SNR per 1.8 km s^{-1} pixel, phase according to equation (1), mean phase of indicated binned spectra, Stokes V detection probability, longitudinal magnetic field and longitudinal field significance, diagnostic null detection probability, longitudinal magnetic field and longitudinal field significance.

Odometer	HJD	Exp (s)	SNR (/pixel)	Phase	$\overline{\text{Phase}}$	P_V (per cent)	$\langle B_z \rangle$	$|z_V|$	P_N (per cent)	$\langle N_z \rangle$	$|z_N|$
1051146	2454844.994	4340	204	0.718							
1051150	2454845.047	4340	204	0.718	0.718	18.179	73 ± 275	0.3	4.580	$+128 \pm 274$	0.5
1513790	2455931.006	4340	264	0.511							
1513798	2455931.084	4340	244	0.513							
1513935	2455931.861	4340	235	0.523							
1513939	2455931.913	4340	238	0.524	0.527	89.468	-253 ± 174	1.5	26.656	$+268 \pm 173$	1.6
1514254	2455933.035	4340	235	0.539							
1514600	2455935.001	4340	266	0.566							
1514818	2455936.014	4340	243	0.580							
1515076	2455936.952	4340	252	0.592	0.589	21.516	-362 ± 186	2.0	68.539	$+144 \pm 186$	0.8
1515397	2455938.928	4340	263	0.619							
1515606	2455940.963	4340	191	0.647							
1516007	2455942.995	4340	265	0.675							
1516011	2455943.048	4340	241	0.675	0.671	25.299	$+300 \pm 170$	1.8	0.028	-104 ± 170	0.6
1516165	2455943.988	4340	259	0.688							
1524346	2455967.882	4340	212	0.014							
1524350	2455967.936	4340	209	0.015							
1524524	2455968.943	4340	204	0.028							
1524528	2455968.997	4340	178	0.029	0.028	68.229	$+422 \pm 223$	1.9	11.331	$+246 \pm 223$	1.1
1524741	2455969.865	4340	233	0.041							
1524745	2455969.918	4340	247	0.042							
1597878	2456259.116	3000	188	0.981							
1597882	2456259.153	3000	168	0.982	0.981	92.015	$+650 \pm 414$	1.6	15.574	$+300 \pm 415$	0.7
1601442	2456283.041	3000	127	0.307							
1601446	2456283.079	3000	128	0.307							
1601450	2456283.116	3000	145	0.308							
1601454	2456283.153	3000	138	0.308	0.327	35.563	-243 ± 168	1.5	0.848	$+51 \pm 169$	0.3
1602166	2456285.940	3000	200	0.346							
1602170	2456285.977	3000	200	0.347							
1602174	2456286.013	3000	205	0.347							
1602178	2456286.050	3000	198	0.348							
1603502	2456290.985	3000	139	0.415							
1603506	2456291.022	3000	131	0.416							
1603510	2456291.059	3000	139	0.416							
1603514	2456291.095	3000	138	0.417	0.416	96.791	-398 ± 361	1.1	27.388	-518 ± 359	1.4
1604359	2456294.875	3000	142	0.468							
1604363	2456294.912	3000	111	0.469							
1604367	2456294.949	3000	107	0.469							
1604371	2456294.986	3000	105	0.470							
1604375	2456295.023	3000	102	0.470	0.470	99.978	$+120 \pm 361$	0.3	84.634	-282 ± 362	0.8
1604379	2456295.060	3000	67	0.471							
1604383	2456295.097	3000	73	0.471							
1604387	2456295.134	3000	76	0.472							

star in the outer part of the disc, beyond the solar circle. The carbon to nitrogen ratio is consistent with little enrichment: N/C < 1.0, compared to 0.25 for the sun (Grevesse et al. 2010). There is no evidence for strong He enrichment. Hence, the abundances of CPD $-28°$ 2561 have barely been affected by chemical processing occurring inside the star.

Finally, we adopted a wind terminal velocity of 2400 km s^{-1}, and a velocity field slope $\beta = 1.0$. These values are typical of O dwarfs/giants. We found that a mass-loss rate of 10^{-6} M$_\odot$ yr^{-1} leads to a density $\rho = \dot{M}_{B=0}/(4\pi r^2 v)$ able to correctly reproduce the shape of Hα in the spectrum showing the weakest nebular contamination. We caution that this value of $\dot{M}$ should not be blindly

interpreted as the true mass-loss rate of this magnetic star's outflow. As discussed in detail in Section 7, the circumstellar structure of CPD $-28°$ 2561 is expected to be highly aspherical and dominated by infalling material. magnetohydrodynamic (MHD) models by ud-Doula et al. (2008) show that for a star like CPD $-28°$ 2561, the true rate of mass lost from the star into interstellar space (i.e. from the top of the magnetosphere) is reduced by a factor of about 5, i.e. ~80 per cent of the material leaving the surface actually falls back upon the star. Hence, the true mass-loss rate is most likely significantly lower than 10^{-6} M$_\odot$ yr^{-1}. Rather, the CMFGEN $\dot{M}_{B=0}$ should be viewed as a parameter giving a first rough estimate of the expected circumstellar density (see further Section 7).
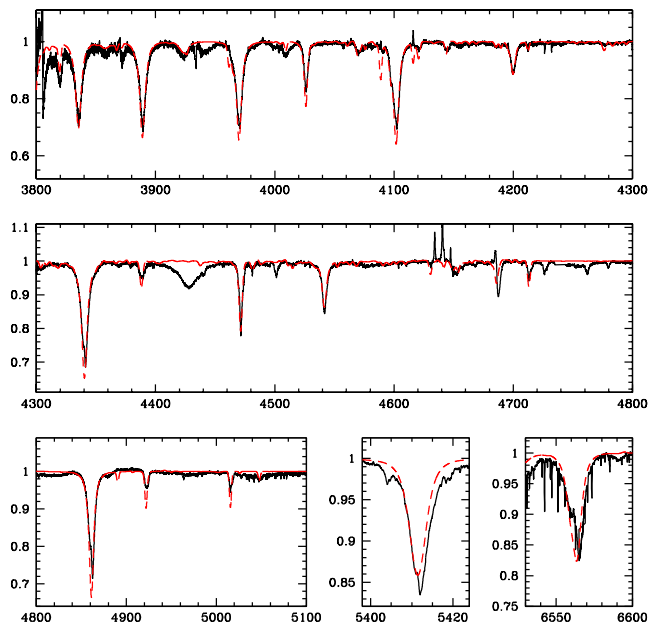
Figure 1. Best-fitting CMFGEN model (red) of the observed ESPaDOnS spectrum (black, phase 0.72, average of spectra #s 1051146/50) for CPD −28° 2561.

4 SPECTRAL VARIABILITY AND PERIOD

Many lines in the spectrum of CPD −28° 2561 show significant variability.

Following a similar analysis as applied by the MiMeS collaboration to other magnetic O-type stars (e.g. Grunhut et al. 2012; Wade et al. 2012a), we first characterize the line variability using the EW. Before measuring the EW, each spectral line was locally re-normalized using the surrounding continuum, and the EWs were computed by numerically integrating over the line profile. The 1σ uncertainties were calculated by propagating the individual pixel uncertainties in quadrature. Pre-computed pixel error bars were only available for the ESPaDOnS and HARPS spectra, which required us to assign a single uncertainty to each pixel for the other spectra that was inferred from the rms scatter of the Stokes *I* flux in the continuum regions around each spectral line.

A period search was performed on the EW measurements from all spectra using the Lomb–Scargle technique (Press et al. 1992) and an extension of this technique to higher harmonics (Schwarzenberg-Czerny 1996). In this approach, a harmonic function with free parameters a_1, a_2, a_0 and P (the latter being the period) corresponding to the form $a_1 \sin(\omega t) + a_2 \cos(\omega t) + a_0$, where $\omega = 2\pi/P$, is fit to the data. Adding the first harmonic leads to the introduction of additional terms of the form $a_3 \sin(2\omega t) + a_4 \cos(2\omega t)$. The resulting periodograms are defined as the power $\sum_{i=1}^{4} a_i^2$ versus period P.

The periodograms (Fig. 2) from the strongly variable lines (such as Hα, Hβ, He I λ5876 and He II λ4686) show significant power at ~36.7 d. When phased with this period, the EW variations show clear sinusoidal variations. However, the sinusoidal variations of the He I λ5876 measurements show considerably more scatter than the other lines. Furthermore, a comparison of spectra obtained at different epochs, but at similar phases according to the ~36.7 d period, shows important differences. These include a systematic velocity offset, a difference in peak emission flux, and opposite skew, of the emission-line profiles. This effect is particularly striking for Hα and He II λ4686, and is illustrated in Fig. 3. Lines in the spectrum of CPD
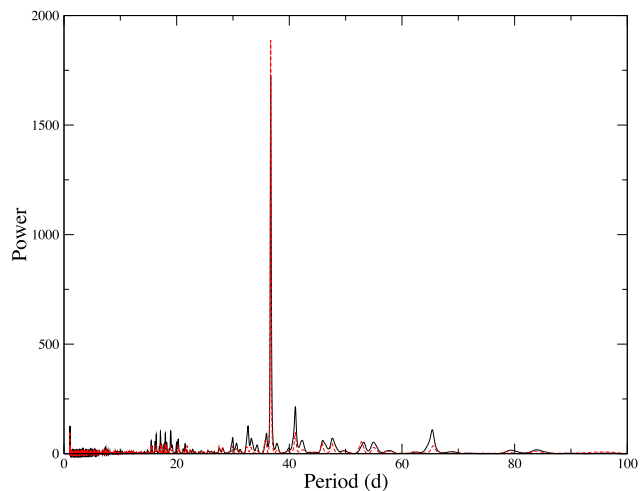

Figure 2. Periodogram obtained from the Hα EW (solid black) and He II λ4686 EW (solid red) measurements. A clear and unique signal at 36.7 d is detected.
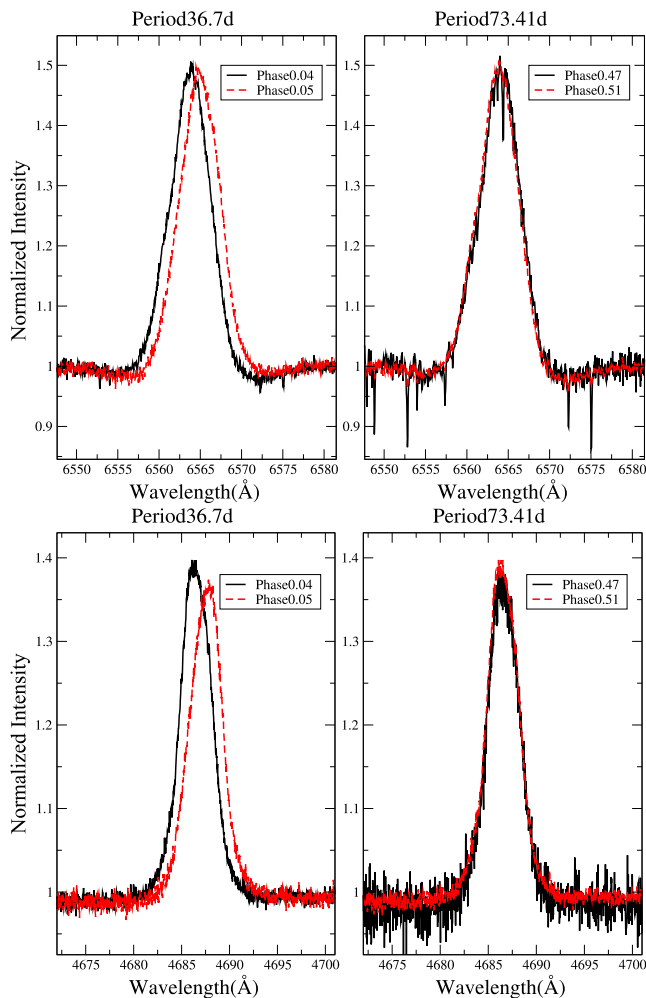

Figure 3. Comparison of Hα and He II λ4686 profiles obtained at similar phases, but at different epochs. Left – assuming a period of 36.7 d, profile shapes at similar phases do not agree. Right – assuming a period of 73.4 d, profile shapes at similar phases agree well. As discussed in the text, we identify the $P = 73.41 \pm 0.05$ as the rotation period based on the better agreement of the profiles at all phases.

$-28°$ 2561 that are primarily in absorption are much more weakly variable; they are therefore poor probes of the wind variability reflected in the emission lines. Nevertheless, the behaviour of lines that are formed deeper in the photosphere (e.g. He II λ4542, C IV $\lambda\lambda$5801, 5811) are indicative of a stable photospheric spectrum that is not plausibly responsible for the phenomenon discussed above.

We therefore carried out a new period search including the contributions from the first harmonic – by including additional harmonics we change not only the relative power in each peak, but also the precise location of the peaks. The resulting periodograms showed two clear peaks, one consistent with the previous periodogram at $\sim$36.7 d and a new peak at 73.41 $\pm$ 0.05 d, twice the previously identified period. When phased with this longer period, the EW variations continue to phase coherently. However, this new phasing achieves a much better agreement between the line profile shapes from spectra corresponding to similar phases, but obtained at different epochs. We therefore conclude that a period of 74.41 d provides a much better solution to the phase variability of CPD $-28°$ 2561, and we adopt this period as the stellar rotation period within the context of a magnetically confined wind and the oblique rotator model (Stibbs 1950; Babel & Montmerle 1997; Wade et al. 2011). Adopting maximum Hα emission (minimum EW) as the reference date we derive the following ephemeris:

$$\text{HJD}_{\text{emis}}^{\text{max}} = 2454645.49(05) + 73.41(05) \times E, \tag{1}$$

where the uncertainties (1σ limits) in the last digits are indicated in brackets. The uncertainties represent the formal 1σ uncertainty computed from the χ^2 statistic corresponding to second-order harmonic fits carried out on the EW variations for periods near 73 d.

The phased EW measurements are illustrated in Fig. 4. The measurements obtained from the various spectral data sets agree reasonably well. Examination of Fig. 4 shows that most lines with significant variability exhibit double-wave variations. Hα shows the most significant variability with a peak-to-peak EW variation of $\sim$5 Å. Maximum emission occurs at phase 0 for most lines, while another emission peak occurs one-half of a cycle later. The value of the EW measurements of Hα and He II λ4686 at maximum emission are similar at both emission maxima, while a higher emission level occurs at phase 0.5 for some other lines (this is most evident in the EW curves of Hβ and He I λ5876), although there is considerable scatter at these phases. Unlike HD 148937, which showed clear variability in C III λ4647 and C IV λ5811 (Wade et al. 2012a), CPD $-28°$ 2561 shows no significant variability in these lines. We also include EWs measured from the DIB at 5797 Å to illustrate the lack of variability of a reference line that is not formed in the environment of the star.

Hipparcos and ASAS data are also available for this star, and we used these data to attempt to detect photometric variability and confirm the derived period. Only the best-quality data were kept: for *Hipparcos*, this means keeping only data with flag 0; for ASAS data, two filterings were used – either keeping only data with grade A (and discarding four strongly discrepant points with $V > 10.1$ mag) or keeping data only at 3σ from the mean (both filtering yielded the same results). Errors amount typically to 0.03 mag for H_p (*Hipparcos*), 0.2 mag for B_T and V_T (*Tycho*), and 0.04 mag for V (ASAS). A χ^2 test for constancy was performed on each data set. Only H_p data were found to be significantly variable with significance level SL $<$ 1 per cent. However, a Fourier period search on those data reveals only white noise, without any significant peaks (or in particular a peak at the expected period of 73.41d). Furthermore, that period does not yield a significant coherent phased variation. Fourier period searches on the *Tycho* data yield similar

conclusions. Period searches [Fourier (Gosset et al. 2001), PDM (Stellingwerf 1978) and entropy (Cincotta, Mendez & Nunez 1995)] on the ASAS data result in the detection of marginal signals with periods of 63.69 $\pm$ 0.13 and 73.43 $\pm$ 0.16 d. The amplitude is very small, $\sim$0.0046 mag at most. When phased with these periods, the photometry only shows marginal variations, even after binning the phased data (Fig. 5). We therefore conclude that any astrophysical variability of the photometric signal is below the typical uncertainty of a few tens of mmag, and would require high-precision photometry to be securely detected.

4.1 Line profile variations

4.1.1 Line profiles of CPD $-28°$ 2561 at high resolution

As discussed above, it is now established that CPD $-28°$ 2561 is the only Of?p star known so far that has double emission-line maxima, corresponding to a geometry that presents both magnetic poles during the rotational cycle. The magnetic O stars HD 47129 (Grunhut & Wade 2013) and HD 57682 (Grunhut et al. 2012) do likewise. In the former case, the complex spectrum of this SB2 system precludes any identification of Of?p characteristics. In the latter case, its wind density is too low to produce the defining He II, C III and N III emission lines, while it does display the characteristic, variable Balmer emission profiles (first noted in a single Hα observation by Walborn (1980). Thus, HD 57682 does provide points of comparison for CPD $-28°$ 2561.

An early indication that the double-wave period of $\sim$73 d is the correct one was provided by the strikingly opposite skews of the He II λ4686 emission peaks at phases 0 and 0.5 (Fig. 6). In addition, there is a velocity offset between the two maximum phases. Both of these effects are also seen in the Balmer emission lines to a lesser degree. Significantly, both effects are likewise seen at Hα in HD 57682. These fine morphological details undoubtedly code significant information about the complex circumstellar structures producing them.

The He II λ4686 and Balmer profiles at the intermediate phases (i.e. at or near 0.25 and 0.75) are also noteworthy but display diversity between the two objects. In CPD $-28°$ 2561, they all have weak emission near the blueward edges of absorption features at both intermediate phases. As already noted, HD 57682 has no λ4686 emission, but remarkably, the Hα profiles have the weak emission components shifted in *opposite* directions at the two intermediate phases. Again, these subtle similarities and differences are important physical clues that need to be modelled and understood.

Turning to the systematic variations of He II λ4686 during the CPD $-28°$ 2561 cycle, some further interesting effects are evident. The weak emission towards the shortward sides of the intermediate-phase profiles gradually strengthens and shifts towards the line centre beginning about 0.3 cycle before each maximum (which again, have opposite skews and a small velocity difference). In contrast, however, the disappearance of the maximum emission lines is remarkably abrupt, occurring within about 0.1 cycle. This behaviour may be suggestive of a sharp occultation of the line-emitting region.

The behaviour of the dilution-sensitive line He I λ5876 is entirely distinct from those of the features just described, which are either similar or opposite between phases 0.5 apart. That of λ5876 is egregiously asymmetrical (Fig. 6): at phase 0.5 it displays a weak absorption flanked by equal emission wings, whereas at phase 0.0 it has a relatively weak but well-marked P Cygni profile. At phases 0.25 and 0.75 it is a strong, symmetrical absorption line.
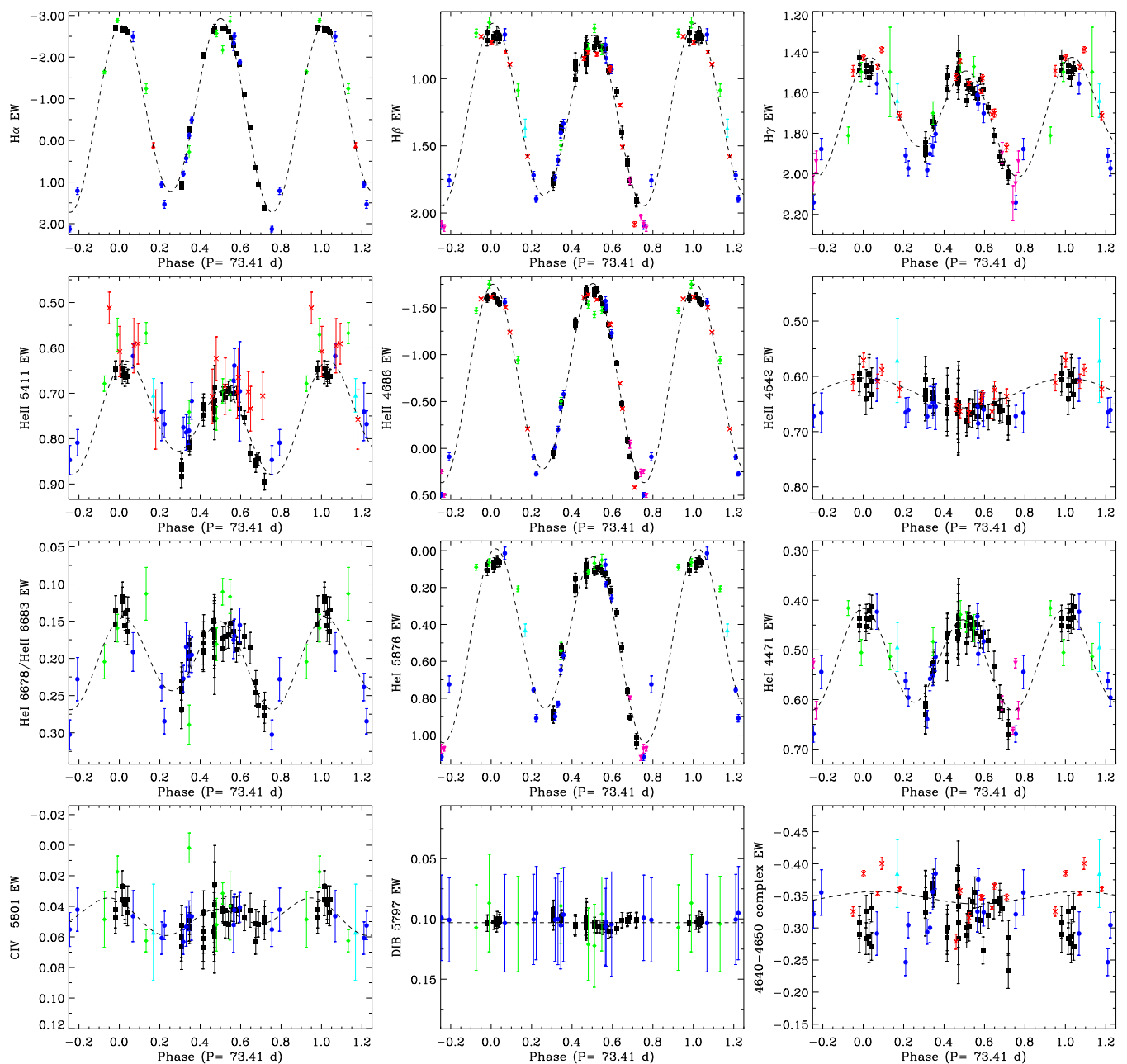
Figure 4. Rotationally phased EW measurements for selected lines in the spectrum of CPD −28° 2561. Least-squares sinusoidal fits are shown for those lines with statistically significant EW variability. In the bottom row, we also show measurements of the λ5797 DIB as an example of an intrinsically non-variable feature. In these figures, the ESPaDOnS measurements are black squares, the HARPS measurement is the cyan upwards facing triangle, the FEROS measurements are the blue circles, the LCO/echelle measurements are the green diamonds, the CAS measurements are the pink downward facing triangles, and the B&C measures are red crosses.

On the other hand, He II λ5411 is a moderate absorption line with strong wings at all phases, which at first glance appears to present velocity shifts opposite to those of the λ4686 and Balmer emission lines at the two maxima. However, on closer inspection the effect is seen to be due to wing emissions in the same sense as those of the other lines, although possibly with a larger amplitude. In contrast, C IV λλ5801, 5812 are weak absorption features with no velocity shifts, albeit with a weak P Cygni tendency at phase 0.0, i.e. in the sense of λ5876. No doubt this apparent chaos will be transformed into valuable diagnostics as our understanding of the intricate phenomenology advances.

Finally, the relative behaviours of He I λ4471 and He II λ4542 (Fig. 6) are of considerable interest, since their ratio is the primary spectral-type criterion, although classification is a heuristic exercise here because of the effects of variable circumstellar emission on the line strengths; the minimum spectrum is expected to be more closely related to the actual stellar parameters. Indeed, both lines are seen to be affected by wing emission at both maxima, albeit the He I line much more strongly. In fact, the λ4542 line has the unique characteristic that its profile at phase ∼0.5 is very similar to that exhibited at the quadrature phases 0.25 and 0.75. Hence, it appears that this line is only affected by one of the emission maxima.
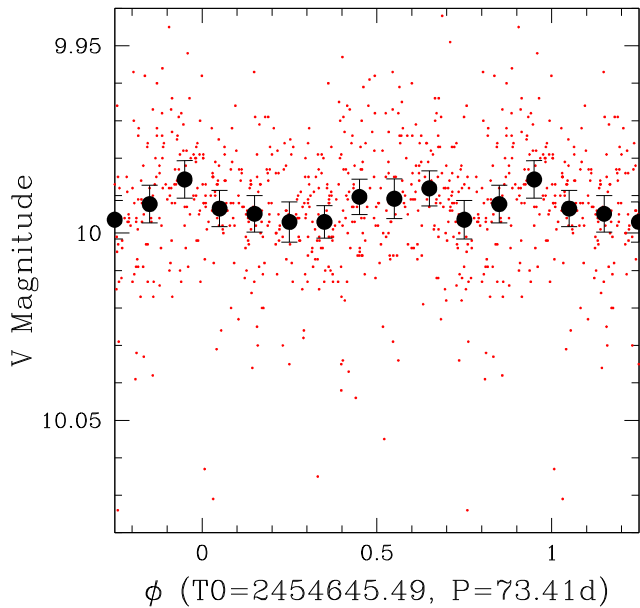
Figure 5. Binned ASAS photometry phased with the spectroscopic ephemeris given by equation (1). Only a marginal variation is detected.

It should be noted that the He I effect is weaker than in other Of?p spectra, whereas the He II one is unprecedented, weaker than but analogous to that in λ5411 described above. In terms of the line depths, the maximum spectral type is O7, but the He II line has

a larger EW so that measurements would yield O6–O6.5. On the other hand, the minimum spectral type is a well-defined O8, which again may be presumed to correspond to the stellar photosphere.

4.1.2 Dynamic spectra

The phased line profile variations are displayed as dynamic spectra in Fig. 7. These images were constructed by subtracting the profile that presented the least overall emission in Hα (corresponding to phase ∼0.75 – obtained on HJD 2454627.467). The colour scheme was chosen to maximize the dynamic range of the variability to highlight changes relative to the minimum profile.

The dynamic spectra of the most strongly variable lines [such as the Balmer lines (Hα, Hβ, Hγ), He I λ5876 and He II λ4686] exhibit very similar characteristics. In each case, the profiles indicate the presence of structures that vary in intensity, from absorption to strong emission, twice per cycle. The two emission features reach similar peak intensities (as already inferred from their EW variations). The emission features of the Balmer lines are slightly asymmetric in velocity about their central peaks and are found to be broad relative to the width of the spectral line (the emission features in Hα have an FWHM of ∼280 km s^{-1}). The emission feature that reaches maximum emission at phase 0 appears to be offset from the mean velocity by about −30 km s^{-1}; the emission feature at phase 0.5 is offset by +30 km s^{-1}.

While the line profile variability in He I λ5876 and He II λ4686 appears similar to the Balmer lines, there are some outstanding
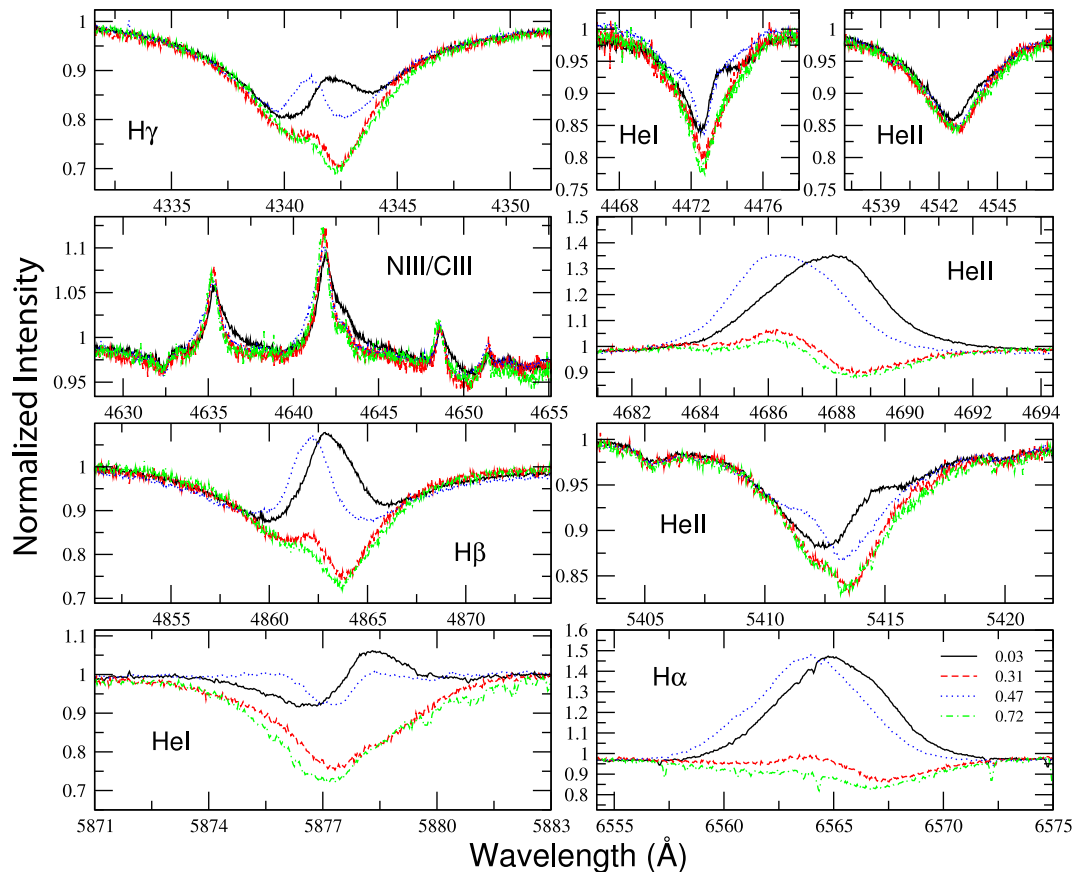

Figure 6. Selected line profiles in the spectrum of CPD −28° 2561 and their variability illustrated near the four principal phases according to the ephemeris derived in Section 4.
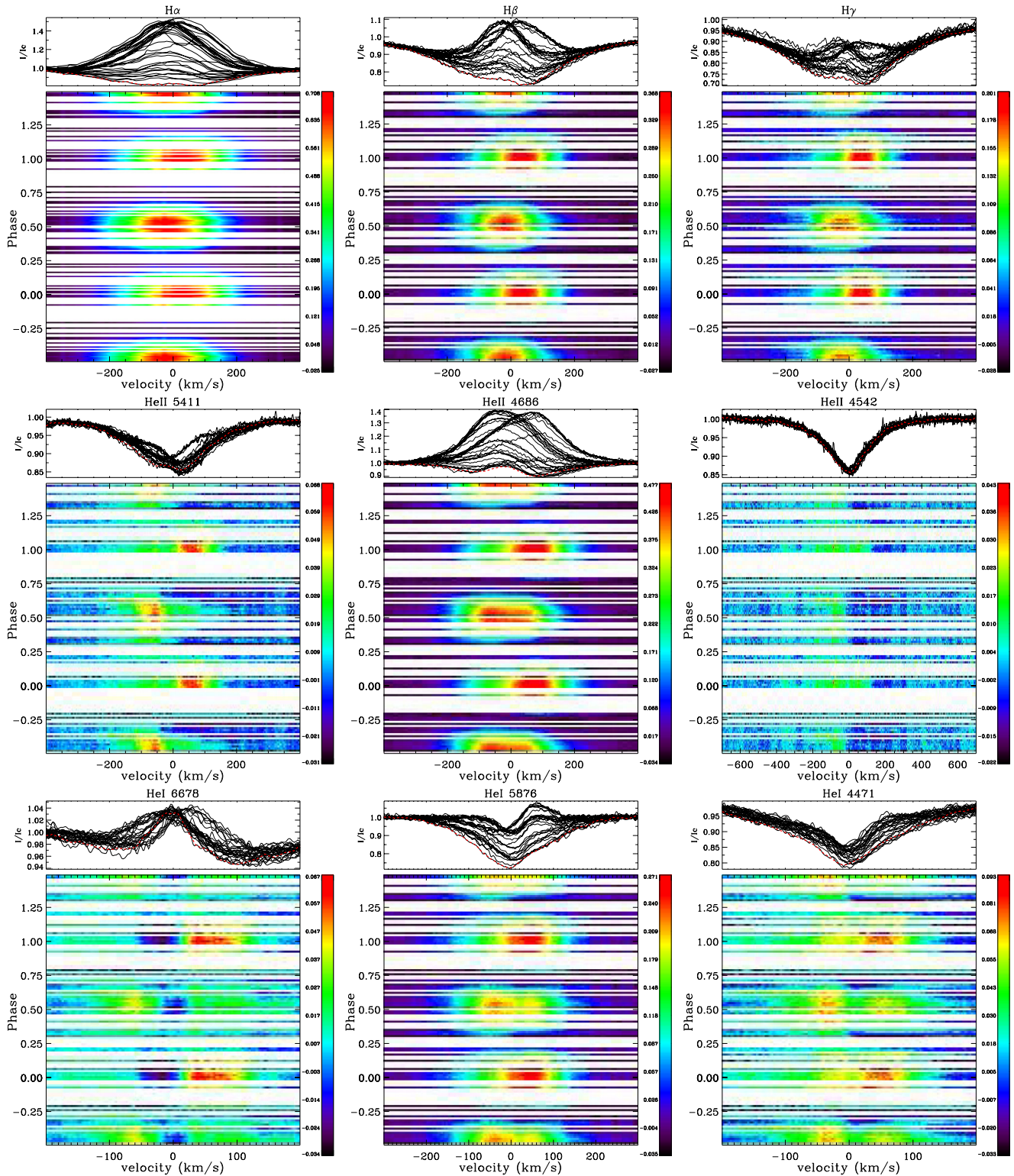
Figure 7. Phased variations of selected spectral lines in the high-resolution spectra, shown as dynamic spectra. Plotted is the difference between the observed profiles and the profile obtained of HJD 2454627.467 (dashed-red, top panel), which occurred at phase ∼0.75, corresponding to minimum observed emission in Hα.

differences. The two emission features appear considerably more asymmetric. In fact, the emission feature occurring at phase 0.5 appears to be a blend of two distinct emission peaks in both lines. The higher intensity peak is centred around −60 km s^{-1} for the

He II line (or −35 km s^{-1} for the He I line), while the less intense peak is centred about 30 km s^{-1} for the He II line (or 50 km s^{-1} for the He I line). While the central velocities of these features differ between these two lines, their separation is similar. The emission

features that appear at phases 0 and 0.5 reach similar peak intensity for the Balmer lines, whereas the intensity of the emission peak at phase 0 is about 10 per cent stronger than the peak occurring at phase 0.5 for the He II line and 20 per cent stronger for the He I line.

The lines that display weaker variability exhibit a character of variability that is similar to those described for the previous lines. The He I λ6678 line shows weaker emission than the previously discussed spectral lines, but there is still evidence for an emission feature occurring twice per cycle. This feature occurs at a velocity relative to the mean velocity that is similar to the other He lines. Furthermore, the relative intensity of the redward emission feature appears considerably stronger than the blueward feature in the He I lines that display less variability (the maximum emission intensity is about 60 per cent stronger than the blueward emission feature of the λ6678 line). Some of the weakly variable lines also show evidence of enhanced absorption (relative to the minimum profile) in a narrow region around the line core. The enhanced absorption reaches a maximum relative absorption in the core at about phase 0.5 (which corresponds to the phase of maximum emission at the blue edge of this line).

The He II λ4542 line exhibits only weak variability. However, it stands out from essentially all other lines in the spectrum of CPD −28° 2561 due to its apparent single-wave variation, a phenomenon reflected in the line profiles examined in Section 4.1.1. In contrast to the double-wave variation of the other lines illustrated in Figs 4 and 7, which show EW maxima at phases 0.0 and 0.5, the λ4542 line appears to exhibit an EW maximum at phase 0.0, but a minimum at phase 0.5.

5 DIAGNOSIS OF THE MAGNETIC FIELD

Least-squares deconvolution (LSD; Donati et al. 1997) was applied to all CFHT observations using the LSD code of Kochukhov, Makaganiuk & Piskunov (2010). In their detection of the magnetic field of HD 191612, Donati et al. (2006) developed and applied an LSD line mask containing 12 lines. Similar masks were successfully employed by Wade et al. (2011, 2012a) in their analyses of HD 191612 and HD 148937. Given the similarity between the spectra of CPD −28° 2561 and HD 191612, we began with this line list and adjusted the predicted line depths to best match the depths observed in the spectrum of CPD −28° 2561 at phases ∼0.25 and 0.75, when the emission is lowest. This involved adjustment of the line depths by typically ∼20 per cent relative to their depths in the spectrum of HD 191612. We then used this line list to extract mean circular polarization (LSD Stokes V), mean polarization check (LSD N) and mean unpolarized (LSD Stokes I) profiles from all collected spectra. All LSD profiles were produced on an 1800 km s^{-1} spectral grid with a velocity bin of 20 km s^{-1}, using a regularization parameter of 0.2 (for more information regarding LSD regularization; see Kochukhov et al. 2010).

Using the χ^2 signal detection criteria described by Donati et al. (1997), we evaluated the significance of the signal in both the Stokes V and N LSD profiles in the velocity range [−150, 250] km s^{-1}, consistent with the observed span of the Stokes I profile. No significant signal was detected in any of the individual V (or N) profiles. We also computed the longitudinal magnetic field from each profile set using equation 1 of Wade et al. (2000a). To improve our sensitivity, we co-added the LSD profiles of spectra acquired within ±2 nights (resulting in nine averages of two to eight spectra, see Table 3). Given the observed variability period (Section 5), ±2 nights corresponds to approximately 0.05 cycles – a timespan

during which variability should be limited; indeed, this was verified empirically. From these profiles, we obtain one marginal detection of signal (false alarm probability, FAP < 10^{-3}) in the V profiles (for the co-added profile corresponding to spectral IDs 1604363–1604387), and best longitudinal field error bars of ∼170 G. The most significant measurement of the longitudinal field from the co-added profiles is −362 ± 186 G (2.0σ). The individual and co-added ESPaDOnS spectra and the corresponding longitudinal fields and detection probabilities are indicated in Table 3. The longitudinal field measured from the HARPSpol spectrum was 280 ± 460 G.

We conclude that we fail to detect a magnetic field in individual and co-added Stokes V spectra of CPD −28° 2561. To proceed further, we note the similarity of the spectrum of CPD −28° 2561 to HD 191612 (and in particular its Of?p classification), and its periodic variability, combined with the reported detection of a strong magnetic field by Hubrig et al. (2011, 2012), strongly suggest that CPD −28° 2561 is an oblique magnetic rotator. This has been convincingly demonstrated for HD 191612 (Wade et al. 2011), and is consistent with the behaviour of other magnetic O-type stars (e.g. Grunhut et al. 2012; Wade et al. 2012a,b).

We therefore proceeded to bin the LSD profiles according to rotational phase as computed via equation (1) in order to increase the SNR. We note that this phase binning implicitly assumes an oblique magnetic rotator, i.e. that the magnetic field variation proceeds according to the same period as the spectra (and other variations). We have binned the co-added LSD profiles from phases 0.307–0.619 and 0.981–0.042. From these profiles (illustrated in Fig. 8), we obtain a definite detection of signal in the Stokes V profile (at phase ∼0.5) and no detection (although with twice poorer SNR) at phase ∼0.0, with no signal detected in the null profiles. Notwithstanding the lack of formal detection at phase 0, the Stokes V LSD profile appears to exhibit a weak signature with polarity opposite to that at phase 0.5. The phase 0.0 and 0.5 LSD profiles yield longitudinal fields of $\langle B_z \rangle = +335 \pm 200$ G and $\langle B_z \rangle = -290 \pm 95$ G, respectively, and corresponding null profile fields of $\langle N_z \rangle = -71 \pm 199$ G and $\langle N_z \rangle = -2 \pm 95$ G. We have also searched the average spectrum at phase ∼0.5 for Zeeman signatures in individual line profiles. Weak signatures, compatible with the LSD Stokes V profiles, are visible in the He I λ5876 and C IV λ5801 lines. We also note that the co-adding LSD profiles phased using one-half the adopted period (i.e. 36.7 d) yields no detection of the magnetic field.

From this analysis, which implicitly assumes that the CPD −28° 2561 is an oblique magnetic rotator, we conclude that an organized magnetic field is detected in the photosphere of CPD −28° 2561, with a longitudinal field with a characteristic strength of several hundred G, which likely changes sign.

6 STELLAR AND MAGNETIC GEOMETRY

With the inferred rotational period and derived radius (from Table 1), CPD −28° 2561 should have an equatorial rotational velocity in the range $v_e \simeq 7$–11 km s^{-1}. Since the upper limit on $v\sin i$ obtained in Section 3 (see Table 4) is much larger than this value due to the significant turbulent broadening of the line profile, we are not able to constrain the inclination of the stellar rotational axis via comparison of v_e and $v\sin i$.

Instead, we derive both the rotational and magnetic geometry of CPD −28° 2561 from considering the rotationally modulated Hα line stemming from the star's hypothetical circumstellar 'dynamical magnetosphere' (Sundqvist et al. 2012). Below the Alfvén radius R_A at which the magnetic and wind energy densities are equal, the magnetic field is strong enough to channel the radiatively-driven
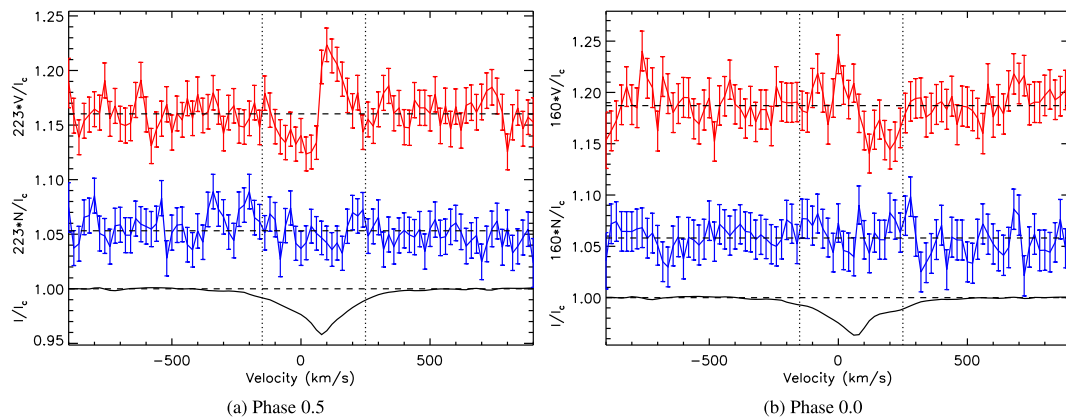
Figure 8. Left: LSD profile at phase 0.5, Stokes *V*: definite detection (FAP = 9e−7 per cent), $\langle B_z \rangle = -290 \pm 95$ G. Diagnostic null *N*: ND (FAP = 72 per cent), $\langle N_z \rangle = -2 \pm 95$ G. Right: LSD profile at phase 0.0, Stokes *V*: no detection (FAP = 2 per cent), $\langle B_z \rangle = +335 \pm 200$ G. Diagnostic null *N*: ND (FAP = 91 per cent), $\langle N_z \rangle = -71 \pm 199$ G.

Table 4. Summary of physical, wind and magnetic properties of CPD −28° 2561. Apart from the luminosity $L/L_\odot$ (which was adopted), all parameters are derived in this paper. The mass-loss rate corresponds to the CMFGEN radiatively-driven rate required to reasonably reproduce the Hα profile; this value is only indicative, since the spherical symmetry assumed by CMFGEN is clearly broken in the case of CPD −28° 2561. The wind magnetic confinement parameter η_*, the rotation parameter *W* and the characteristic spin-down time $\tau_{\rm spin}$ are defined and described in Section 7. Values in brackets for η_*, $R_{\rm A}$ and $R_{\rm K}$ correspond to the best-fitting parameters.

Spectral type	Of?p
$T_{\rm eff}$ (K)	$35\,000 \pm 2000$
$\log g$ (cgs)	4.0 ± 0.1
R_* ($R_\odot$)	12.9 ± 3.0
$\log (L_*/L_\odot)$	5.35 ± 0.15
$M_{\rm evol}$ ($M_\odot$)	35 ± 6
$M_{\rm spec}$ ($M_\odot$)	61 ± 33
$v \sin i$ (km s^{-1})	$\lesssim 80$
$P_{\rm rot}$ (d)	73.41 ± 0.05
$\log \dot{M}_{B=0}$ ($M_\odot$ yr^{-1})	-6.0
v_∞ (km s^{-1})	2400
$B_{\rm d}$ (G)	2600 ± 900
i (°)	35 ± 3
β (°)	90 ± 4
η_*	20–900 (93)
$R_{\rm A}$ (R_*)	2.1–5.5 (3.4)
$R_{\rm K}$ (R_*)	14.2–29.9 (18.7)
$\tau_{\rm spin}$	0.45 Myr
N/H	$< 5 \times 10^{-5}$
C/H	$(5 \pm 3) \times 10^{-5}$

wind outflow of CPD −28° 2561 along closed field lines (ud-Doula & Owocki 2002). The trapped wind plasma, channelled along field lines from opposite magnetic hemispheres then collides at the magnetic equator, and is pulled back to the star's surface by gravity. This in turn leads to a statistically overdense region centred around the magnetic equator, which is also characterized by infalling material of quite low velocities (as compared to non-magnetic O star wind velocities). If the magnetic and rotational axes of the star are mutually inclined, an observer at earth will view this dynamical magnetosphere from different perspectives, which leads to rotationally modulated line profiles (Grunhut et al. 2012; Sundqvist et al. 2012; Petit et al. 2013; ud-Doula et al. 2013). Below we use this variability to derive constraints on the magnetic geometry of CPD −28° 2561.

We follow the procedure developed by Sundqvist et al. (2012, see also Grunhut et al. 2012 and ud-Doula et al. 2013) and use 100 snapshots of a 2D radiation MHD wind simulation of a magnetic O-star, that we patch together in azimuth to form a 3D 'orange slice' model. The MHD simulation employed here is that computed for HD 191612 (see Sundqvist et al. 2012) as a proxy for CPD −28° 2561. This is a reasonable approach because both HD 191612 and CPD −28° 2561 are slow rotators (in the sense that rotation is dynamically insignificant in determining the wind/magnetosphere properties), and their magnetic field strengths/confinement parameters are formally identical (see Section 7). Hence, the geometry of the plasma confinement should be similar in both cases (ud-Doula & Owocki 2002).

The tests by ud-Doula et al. (2013) show this patching technique results in a reasonably good representation of the full 3D magnetosphere. To compute synthetic Hα spectra, we then solve the formal solution of radiative transfer in a 3D cylindrical system for an observer viewing from angle α with respect to the magnetic axis. For magnetic obliquity β and observer inclination *i*, we then have

$$\cos \alpha = \sin \beta \cos \Phi \sin i + \cos \beta \cos i, \qquad (2)$$

which gives the observer's viewing angle as function of rotational phase Φ, thus mapping out the rotational phase variation for a given couple of β and *i*.[3] We solve the formal solution only in the wind, assuming Hα occupation numbers and a temperature structure given by a 1D NLTE model atmosphere calculation, and using an input photospheric Hα line profile as lower boundary condition (see

---

[3] Although the 2D MHD simulations of ud-Doula & Owocki (2002) assumed field-aligned rotation, the slow rotation of CPD −28° 2561, and hence the lack of any significant dynamical influence of rotation, allows us to construct 3D non-aligned structures for synthesis of Hα.
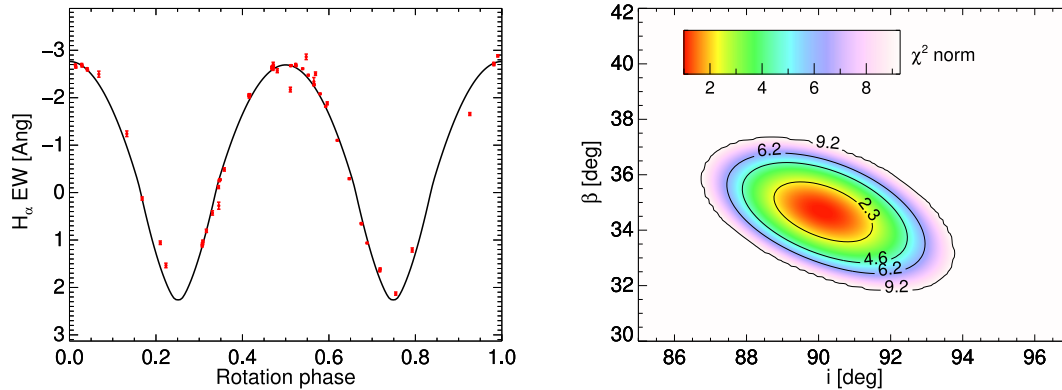
Figure 9. MHD modelling of the Hα variation. Left – model fit to the phased Hα EW variation. Right – χ^2 contour map illustrating the best-fitting solution of the magnetic geometry. See text for details.

Sundqvist et al. 2012 for more details). The infalling material in our selected 100 snapshots falls preferably towards one pole. This is most presumably due to a subtle numerical issue in the MHD simulations, where over a time this north–south asymmetry is cancelled out (see ud-Doula & Owocki 2002). To account for the fact that in these non-rotating stars there should be no preference between the north and south magnetic pole, we here average computed line profiles from the same angle α as counted from the north and south magnetic poles, respectively.

The absolute level of Hα emission should further, in principle, provide constraints on the rate by which the magnetosphere is fed by radiatively-driven wind material (in analogy with how Hα emission from non-magnetic O-stars provides constraints on the stellar mass-loss). However, as discussed in detail by Grunhut et al. (2012), adjusting the underlying model so that the level of Hα emission is reproduced in the high-state results in variability between the high and low states that is too small to reproduce the observations. Since here we are mainly interested in obtaining constraints on the magnetic geometry from the variability itself, we thus compute synthetic Hα EW curves that have somewhat too strong absolute emission and then simply shift them down so that the absolute level of emission at the extrema are fit. This then results in EW curves that reproduces well the variability, providing good constraints on the geometry. However, because of this shifting we are not able to simultaneously derive constraints on the mass feeding rate; this issue will be discussed in detail in a forthcoming paper.

The right-hand panel of Fig. 9 shows the χ^2 landscape from fitting the observed rotational phase variation for given sets of β and i. Because of the strong emission dependence on α, the error bars of the best fit $i = 90$ deg and $\beta = 35$ deg are quite small. We note however that simply switching the obliquity and inclination angles gives equal results, i.e. there is a second 'best-fitting' model at $i = 35$ deg and $\beta = 90$ deg (that is not shown in the figure). The left-hand panel then finally compares the best model with the observed variability as function of rotational phase.

6.1 Photometric and broad-band polarization variability

A second constraint on the geometry is potentially derived from photometric and broad-band (linear) polarimetric variability. We use the Monte Carlo radiative transfer (RT) code developed by RHDT for simulating light scattering in circumstellar envelopes, first applied in this context to the Of?p star HD 191612 by Wade

et al. (2011). In this code, photon packets are launched from a central star and allowed to propagate through an arbitrary distribution of circumstellar matter (described by a Cartesian density grid), until they are scattered by free electrons. Upon scattering, a ray is peeled off from the packet towards a virtual observer, who records the packet's Stokes parameters appropriately attenuated by any intervening material (see Yusef-Zadeh, Morris & White 1984, for a discussion of this peel-off technique). A new propagation direction is then chosen based on the dipole phase function (Chandrasekhar 1960), and the packet's Stokes parameters are updated to reflect the linear polarization introduced by the scattering process. The propagation is then resumed until, after possible further scatterings, the packet eventually escapes from the system or is reabsorbed by the star.

We employ the circumstellar density model developed for HD 191612, and compute light curves for the two geometries derived from the orange-slice MHD modelling. In Fig. 10, we compare the observed ASAS V-band photometric variation with the predictions of the Monte Carlo RT code. Unfortunately, the available photometry is not sufficiently precise to allow us to obtain meaningful constraints on the geometry. Nevertheless, the predictions demonstrate that the existing photometry is at the threshold of being able to detect the predicted variation. High-precision photometry and broad-band polarimetry would provide an additional constraint on the geometry, and in particular the polarimetric variation would enable the determination of the individual values of the angles i and β.

6.2 Longitudinal magnetic field variation

To infer the strength of the magnetic field, and to test its compatibility the derived geometry, we model the longitudinal field variation of CPD $-28°$ 2561 as a function of rotational phase. We used the co-added profiles discussed in Section 5 and reported in Table 3, phased according to equation (1). This phase variation $\langle B_z \rangle(\phi)$ of the longitudinal field is illustrated in Fig. 11 (upper frame). A fit by least-squares of a cosine curve of the form $\langle B_z \rangle(\phi) = B_0 + B_1 \cos(2\pi(\phi - \phi_0))$ to the data yields a reduced χ^2 of 0.84, with parameters $B_0 = +115 \pm 55$ G, $B_1 = 450 \pm 100$ G and $\phi_0 = 0.18 \pm 0.15$.

Therefore, according to least squares, the variation of the field is detected at 4.5σ confidence. The reduced χ^2 of the data relative to the straight line $\langle B_z \rangle(\phi) = 0$ (the hypothesis of a null field) is

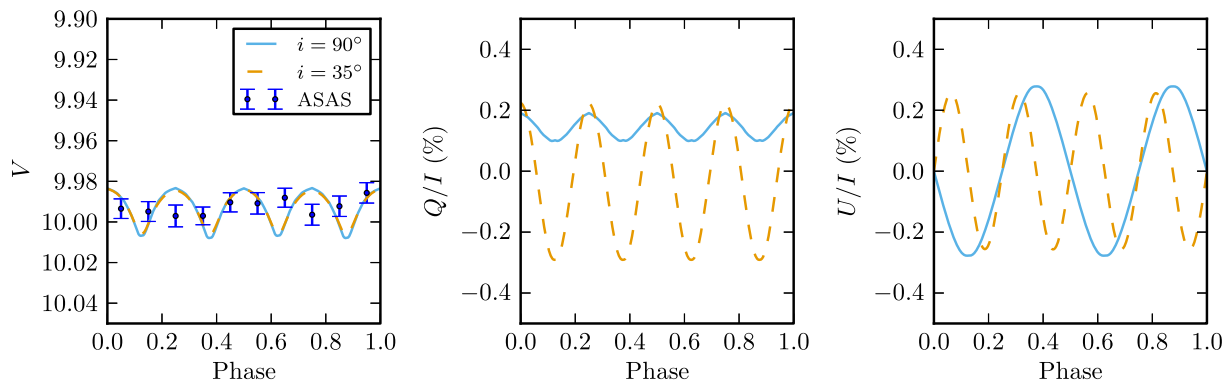**Figure 10.** Predicted light-curve and broad-band polarization variations of CPD −28° 2561. Variations are shown for two models: ($i = 35°$, $\beta = 90°$), and ($i = 90°$, $\beta = 35°$). Whereas both models produce identical light curves, their polarization variations are clearly distinct.
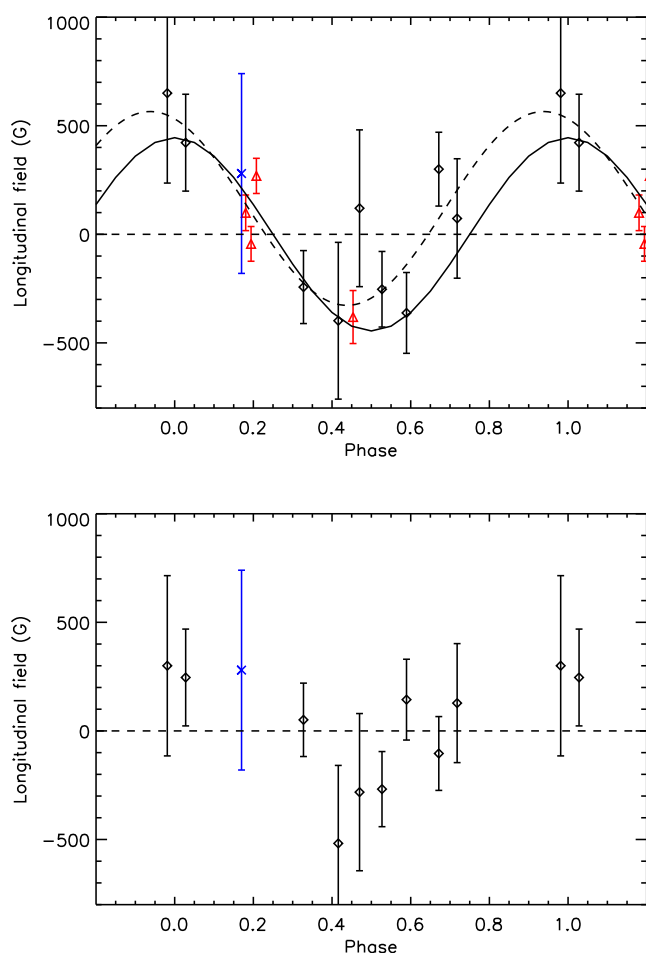

Figure 11. Top panel: longitudinal field versus phase. Dashed line – best-fitting sinusoid. Solid line – dipole model (fixed phase and geometry, polar strength $B_d = 2.6$ kG). Diamonds represent ESPaDOnS measurements from the current study. The cross is the HARPSpol measurement. The triangles are measurements from Hubrig et al. (2011, 2013). Bottom panel: null field versus phase. All measurements are phased according to equation (1).

2.3. These results indicate that the variation is significant at about 97 per cent confidence, and that the null hypothesis can be rejected as an acceptable representation of the data at similar confidence. The longitudinal field measured from the null profiles (lower frame

of Fig. 11) yields similar reduced χ^2 for both the cosine and straight-line fits, and indicates no significant variation.

Adopting $i = 35°$ and $\beta = 90°$ from the modelling of the Hα EW, we have fitted the phase-binned longitudinal field measurements with a synthetic longitudinal field variation with fixed phase of maximum (phase 0.5) and variable polar field strength B_d. The best-fitting model (according to the χ^2 statistic) is characterized by $B_d \simeq 2.6$ kG. The extrema of the best-fitting dipole model are slightly offset from the best-fitting sinusoid in mean longitudinal field strength (by about 100 G) and in phase (by about 0.07 cycles). These offsets are well within the uncertainties of the observed variation. Taking them into account, we estimate an uncertainty on the derived dipole strength of ±900 G.

If we fix only the inclination and allow both β and B_d to vary, a direct fit to the longitudinal field variation yields best-fitting values of $\beta = 78^{+10°}_{-8}$ and $B_d = 2.7 \pm 1.1$ kG. These values are in good agreement with those derived from the fit with fixed geometry derived above.

In Fig. 11, we also show the longitudinal field measurements of Hubrig et al. (2011, 2013) obtained from 'all' lines. Those measurements, which have formal errors that are substantially more precise than our own, are in good agreement with both the best-fitting synthetic dipole and the best sinusoidal fit. It is notable that three of the measurements of Hubrig et al. were acquired at essentially the same phase, which corresponds to crossover (i.e. $\langle B_z \rangle \simeq 0$).

6.3 Modelling the Stokes *V* profiles

We also modelled the magnetic field geometry using the LSD Stokes *V* profiles. We compared the mean LSD profiles for phases 0.0, 0.5 and 0.75 to a grid of synthetic Stokes *V* profiles using the method of Petit & Wade (2012). For this modelling, we used LSD profiles extracted using a metallic line mask, as described by Wade et al. (2012a).

The emergent intensity at each point on the stellar surface is calculated using the weak-field approximation for a Milne–Eddington atmosphere model. In this model, the source function is linear in optical depth such that $S(\tau_c) = S_0[1 + \beta\tau_c]$. We use $\beta = 1.5$, Voigt-shaped line profiles with a damping constant $a = 10^{-3}$ and a thermal speed $v_{th} = 5$ km s^{-1}. The line-to-continuum opacity ratio κ is chosen to fit the intensity LSD profile. The synthetic flux profiles are then obtained by numerically integrating the emergent intensities over the projected stellar disc. The projected rotational

Table 5. Odds ratios derived from the analysis of Stokes *V* profiles.

Phase	$\log(M_0/M_1)$ V	$\log(M_0/M_1)$ N
0.00	−0.91	0.09
0.50	−7.43	0.24
0.75	−0.34	0.06
Combined	−9.06	0.25

velocity is set to $v\sin i = 9$ km s^{-1}. We applied isotropic Gaussian macroturbulence[4] compatible with that determined in Section 3.

We assume a simple centred dipolar field, parametrized by the dipole field strength B_d, the rotation axis inclination i with respect to the line of sight, the positive magnetic axis obliquity β and the rotational phase φ. Assuming that only φ may change between different observations of the star, the goodness-of-fit of a given rotation-independent (B_d, i, β) magnetic configuration can be computed to determine configurations that provide good posterior probabilities for all the observed Stokes *V* profiles in a Bayesian statistic framework. In order to stay general, we do not at this point constrain the rotational phases of the observations nor the inclination of the rotational axis.
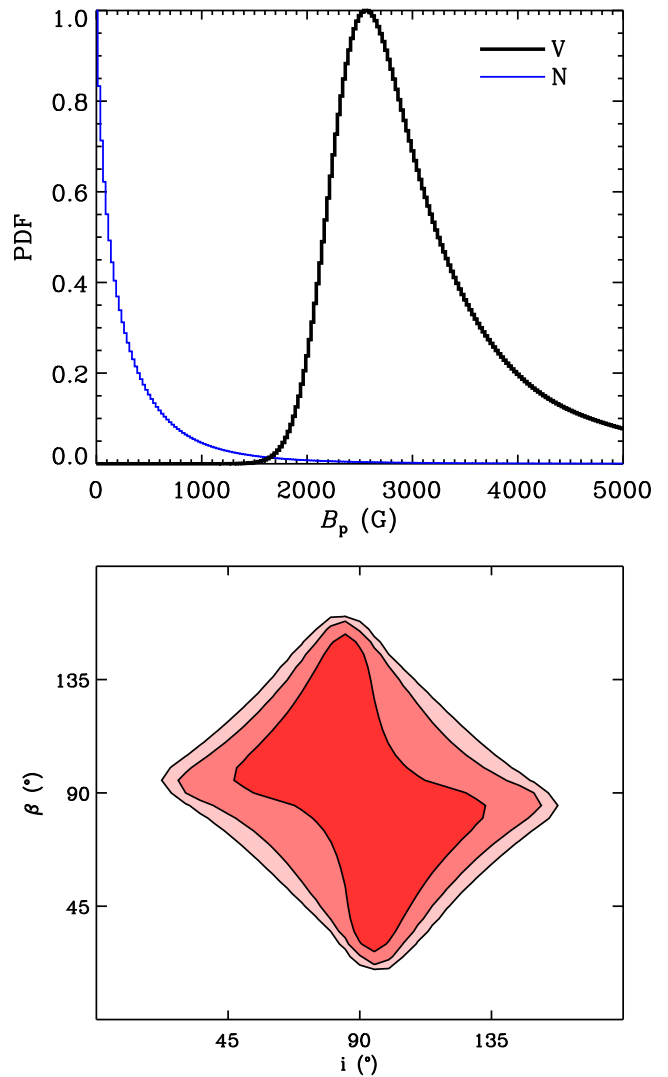
The Bayesian prior for the inclination is described by a random orientation [$p(i) = \sin(i)\,di$], the prior for the dipolar field strength has a modified Jeffreys shape to avoid a singularity at $B_d = 0$ G, and the obliquity and the phases have flat priors.

To assess the presence of a dipole-like signal in our observations, we compute the odds ratio of the dipole model (M_1) with the null model (M_0; no magnetic field implying Stokes $V = 0$). We also perform the same analysis on the null profiles. The results are displayed in Table 5. Taking into account all the observations simultaneously, the odds ratio is in favour of the magnetic model by nine orders of magnitude. For the null profiles, the combined odds ratio is 2:1 in favour of the null model. Note that as the case $B_d = 0$ G is included in the magnetic model, in the latter case the difference between the two models, which can equally well reproduce a signal consisting of only pure noise, is expected to be dominated by the ratio of priors in this case, i.e. the Occam factor that penalizes the magnetic model for its extra complexity.

Fig. 12 shows the posterior probability density function for each model parameters. The 68.3, 95.4, 99.0, and 99.7 per cent regions, tabulated in Table 6, are illustrated in dark to pale shades, respectively. At 95.4 per cent confidence, the polar strength of the dipole magnetic field of CPD −28° 2561 is found to be in the range $1.9 \leq B_d \leq 4.5$ kG. This is in good agreement with the dipole strengths derived from the longitudinal field variation.

Figure 12. Magnetic field polar strength (upper frame) and geometry (i, β) (lower frame) constraints derived from of modelling of Stokes *V* profiles.

Table 6. Credible regions derived from the Bayesian analysis of Stokes *V* profiles.

Credible region	Range in gauss
	V
99.7	1754–5000
99.0	1841–4947
94.5	1891–4509
68.3	2137–3307
	N
99.7	0–3835
99.0	0–2767
95.4	0–1508
68.3	0–425

7 MAGNETOSPHERE

As presented by ud-Doula & Owocki (2002), the global competition between the magnetic field and stellar wind can be characterized by the so-called wind magnetic confinement parameter $\eta_* \equiv B_{\rm eq}^2 R_*^2 / \dot{M}_{B=0} v_\infty$, which depends on the star's equatorial field strength ($B_{\rm eq}$), stellar radius (R_*), and wind momentum ($\dot{M}_{B=0} v_\infty$) the star would have in absence of the magnetic field. For a dipolar field, one can identify an Alfvén radius $R_A \simeq \eta_*^{1/4} R_*$, representing the extent of strong magnetic confinement. Above R_A, the wind dominates and stretches open all field lines. But below R_A, the wind

---

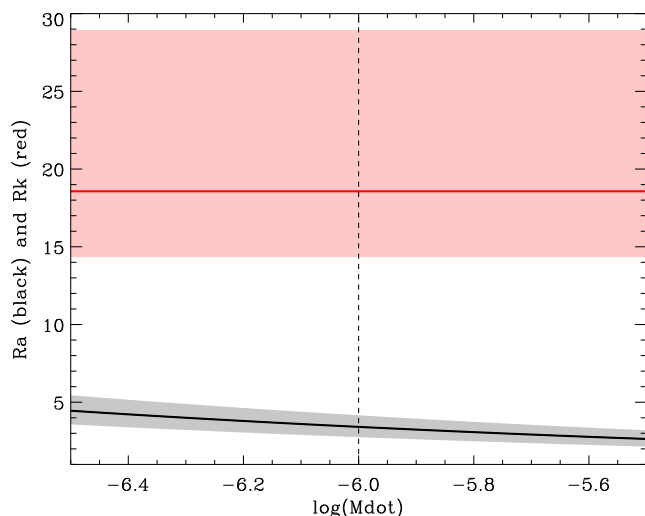[4] of the form $e^{-v^2/v_{\rm mac}^2}/(\sqrt{\pi} v_{\rm mac})$.

Figure 13. Alfvén (black, lower curve) and Kepler (red, upper curve) radii as a function of the mass-loss rate.

material is trapped by closed field line loops, and in the absence of significant stellar rotation is pulled by gravity back on to the star within a dynamical (free-fall) time-scale.

To estimate the Alfvén radius of the magnetosphere of CPD −28° 2561, we use the stellar parameters given in Table 4.

The stellar parameter with the largest uncertainty is the wind momentum. Fig. 13 therefore illustrates the variation of R_A with one order of magnitude variation in mass-loss rate (corresponding to a generous estimate of the uncertainty). One can see how this uncertainty is mitigated by the 1/4 power dependence of the wind momentum in the definition of the Alfvén radius. The grey shaded areas represent intervals of stellar radius uncertainty (± 3 R$_\odot$) and of dipole field strength (2.1, 2.6, 3.3 kG, reflecting the 68.3 per cent Bayesian credible region) meant to minimize and maximize the Alfvén radius.

We therefore expect the Alfvén radius to be of the order of 3 stellar radii, and certainly no more than 5 stellar radii.

In the presence of significant stellar rotation, centrifugal forces can support any trapped material above the Kepler corotation radius $R_K \equiv (GM/\omega^2)^{1/3}$. This requires that the magnetic confinement extend beyond this Kepler radius, in which case material can accumulate to form a *centrifugal magnetosphere* (e.g. Townsend, Owocki & Groote 2005).

In the case of CPD −28° 2561, the slow rotation puts the Kepler radius much farther out than the Alfvén radius (~ 18 R$_*$) and no long-term accumulation of wind plasma is expected, as illustrated by the red curve in Fig. 13 (the red shaded area represents ± 3 R$_\odot$ and a range of mass from 30 to 60 M$_\odot$). In such a *dynamical magnetosphere* configuration, transient suspension of circumstellar material results in a statistical global overdensity in the closed loops. For O-type stars with sufficient mass-loss rates, the resulting dynamical magnetosphere can therefore exhibit strong emission in Balmer recombination lines (Sundqvist et al. 2012; Petit et al. 2013). This conclusion supports the MHD modelling employed to determine the stellar geometry in Section 6. We note that due to infalling wind material (which may be reflected in the P Cyg-like profile of He II λ4686 at some phases), the global mass-loss rate of a star exhibiting such a dynamical magnetosphere is significantly reduced. According to the scaling relations of Ud-Doula, Owocki & Townsend (2008) (their equations 10 and 23), for an estimated $R_A \approx 3R_*$, $\dot{M}/\dot{M}_{B=0} \approx 0.2$, i.e. the global mass-loss rate is reduced

by approximately a factor of 5 due to wind plasma falling back upon the star.

The characteristic magnetic braking time can be estimated using equation 25 of ud-Doula, Owocki & Townsend (2009). Using the nominal wind parameters in Table 4 and $k \sim 0.1$ (Claret 2004), we obtain a spin-down time-scale of 0.45 Myr. However as noted by Petit et al. (2013), the square-root dependence of this quantity on the wind momentum renders spin-down estimates valid only to a factor of a few.

8 DISCUSSION AND CONCLUSIONS

In this paper, we have performed a first thorough analysis of the variability, geometry, magnetic field and wind confinement of the Of?p star CPD −28° 2561. Using more than 75 new medium and high resolution spectra, we determined the EW variations and examined the dynamic spectra of photospheric and wind-sensitive spectral lines, deriving a rotational period of 73.41 d. We confirmed the detection of an organized magnetic field via Zeeman signatures in LSD Stokes *V* profiles. The phased longitudinal field data exhibit a weak sinusoidal variation, with maximum of about 565 G and a minimum of about −335 G, with extrema approximately in phase with the Hα EW variation. Modelling of the Hα EW variation assuming a 3D 'orange-slice' magnetospheric model yields a unique solution for the ambiguous couplet of inclination and magnetic obliquity angles: (i, β) or $(\beta, i) = (35°, 90°)$. Assuming this geometry, the surface magnetic field dipole strength is inferred to be $B_d = 2.6 \pm 0.9$ kG. The magnetic strength and rotational period of CPD −28° 2561 are rather typical for magnetic O-type stars.

Using the magnetic field strength and inferred wind properties, we derive the wind magnetic confinement parameter $\eta_* \simeq 93$, yielding an Alfvén radius $R_A \simeq 3.4R_*$, and a Kepler radius $R_K \simeq 18.7R_*$. This supports a picture in which the Hα emission and other line variability have their origin in an oblique, corotating 'dynamical magnetosphere' structure resulting from a magnetically channelled wind. This framework is consistent with that inferred for the other Galactic Of?p stars HD 108 (Martins et al. 2010), HD 148937 (Wade et al. 2012a), HD 191612 (Donati et al. 2006; Wade et al. 2011) and NGC 1624−2 (Wade et al. 2012b) as well as the cooler magnetic O-type star HD 57682 (Grunhut et al. 2012). The computed spin-down time of CPD −28° 2561 (equal to 0.45 Myr) is similar to that of HD 191612 (0.33 Myr). On the other hand, it is significantly shorter than that of HD 148937 (Wade et al. 2012a). At face value, it is also significantly shorter than that of HD 108 (1–3 Myr; Martins et al. 2010); however, the value for HD 108 is based on a highly uncertain estimate of the polar field strength. Considering the large range of rotational periods of these stars, and the general lack of accurate information concerning their ages, it is as yet difficult to derive any meaningful conclusions about the role of magnetic braking in the evolution of these stars.

Most lines in the spectrum of CPD −28° 2561 are detectably variable, including lines of H, He I/II, and (more weakly) C IV. The EW variation of most lines is 'double-wave', exhibiting two maxima (and minima) per rotational cycle. The EW variability and extrema of most lines are roughly symmetric in both phase and amplitude, although the maximum/minimum at phases 0.25/0.5 are somewhat (10–20 per cent) less pronounced in some lines than those at phases 0.75/0.0. The He II λ4542 line is the only line investigated that exhibits apparently 'single-wave' variability. The double-wave nature of the variations of most lines can be naturally explained as the consequence of the stellar and magnetic geometry of CPD −28° 2561: the derived inclination and obliquity angles yield

$i + \beta = 135°$, implying that both magnetic poles are presented clearly to the observer during each stellar rotation. Only two other magnetic O-type stars are known to exhibit analogous behaviour: HD 57682 (Grunhut et al. 2012), for which $i + \beta = 139°$, and Plaskett's star (e.g. Grunhut & Wade 2013, and Grunhut et al., in preparation), for which $i + \beta \simeq 130°$.

The behaviour of the $\lambda 4542$ line can likely be understood as due to the depth of formation and the relative contribution of the magnetosphere to the line profile. Martins et al. (2014) constrained the line formation region of various lines in spectra of non-magnetic O stars, and investigated the variability as a function of depth. They demonstrate that the Balmer lines are formed further out in the wind compared to some weak He I or high-ionization He II or C IV lines. Lines formed closer to the photosphere also exhibit some additional variability that likely arises in the photosphere (and this may qualitatively explain the different behaviour of lines such as He II $\lambda 4542$). However, the variability of these photospheric lines is weak in comparison to the variability of wind-dominated lines, and cannot contribute appreciably to the variability of features such as Hα or He II $\lambda 4686$. We therefore propose that in the case of CPD $-28°$ 2561 (and likely other magnetic O stars), lines clearly formed out in the magnetosphere (Hα, Hβ, He II $\lambda 4686$) are overwhelmingly dominated by the rotational variation of the density of the confined wind plasma.

The dynamic spectra of CPD $-28°$ 2561 reveal characteristic differences in the mean velocities and skewness of the two emission maxima per rotation cycle. This phenomenon – first discussed by Grunhut et al. (2012) in the context of HD 57682 – is not reproduced by the orange-slice MHD model. In the case of HD 57682, the shift between the two emission peaks is about 70 km s^{-1}; for CPD $-28°$ 2561, it is comparable (about 60 km s^{-1}). This effect could potentially be explained by a difference in strength and/or geometry of the two magnetic poles at the stellar surface. Such differences are commonly inferred for cooler magnetic stars and are frequently parametrized using a dipole model offset from the stellar centre along its axis. Typically, dipole offsets measured for Ap/Bp stars are 0.0–0.3R_* (e.g. Wade et al. 1997, 2000b). First, 2D MHD simulations computed using reasonable dipole offsets provide promising results. However, their presentation and discussion is outside the scope of this paper. This potential ability of dipole offset to explain the observed emission-line variations will be the topic of a forthcoming paper.

The absolute level of Hα emission from the magnetosphere of an O star should provide constraints on the rate by which it is fed by radiatively-driven wind material through comparison with theoretical models such as those described in Section 6. However, as discussed in detail by Grunhut et al. (2012), adjusting the underlying MHD model so that the level of Hα emission is reproduced in the high-state results in variability between the high and low states that is too small to reproduce the observations. This was interpreted by those authors as a consequence of a magnetosphere consisting of somewhat optically thicker plasma 'snakes' (dense plasma clumps falling back towards the star) than predicted by 2D MHD models. Such thicker clumps would lead to higher variability at a given mass-loss feeding rate, and so to a better fit to the observations for the mass-loss feeding rate that reproduces the mean level of emission in the high state.

For CPD $-28°$ 2561, we reproduced the EW variation of the Hα line by computing synthetic Hα EW curves with somewhat too strong absolute emission and then artificially shifting them so that the absolute levels of emission at the extrema were fit. While this procedure resulted in EW curves that reproduced well the variabil-

ity, we were not able to simultaneously derive constraints on the mass feeding rate. Recent monitoring of CPD $-28°$ 2561 has been performed with *Hubble Space Telescope*/STIS (UV spectroscopy) and *XMM* (X-ray spectroscopy) [PI: Nazé]. These data will likely help to mitigate the problem of the star's uncertain wind properties, and will provide important insights into its wind confinement and magnetosphere.

In conclusion, we underscore that the weak longitudinal magnetic fields, complex spectra and faint apparent magnitudes of all Of?p stars challenge the capabilities of current polarimetric instrumentation. While their magnetic fields are securely detected, field topologies are only very roughly characterized. The subject of this paper – CPD $-28°$ 2561 – along with HD 148937, represent the most challenging examples of the class. The development of spectropolarimetric capabilities such as those of ESPaDOnS, but on 8 m-class telescopes, is an vital step required in order to investigate stars such as these at an acceptable level of detail, and more generally to extend our understanding of the magnetic properties of the most massive stars.

REFERENCES

Babel J., Montmerle T., 1997, ApJ, 485, L29
Barbá R. H., Gamen R., Arias J. I., Morrell N., Maíz Apellániz J., Alfaro E., Walborn N., Sota A., 2010, Rev. Mex. Astron. Astrofis., 38, 30
Chandrasekhar S., 1960, Radiative Transfer. Dover Press, New York
Cincotta P. M., Mendez M., Nunez J. A., 1995, ApJ, 449, 231
Claret A., 2004, A&A, 424, 919
Donati J.-F., Semel M., Carter B. D., Rees D. E., Collier Cameron A., 1997, MNRAS, 291, 658
Donati J.-F., Howarth I. D., Bouret J.-C., Petit P., Catala C., Landstreet J., 2006, MNRAS, 365, L6
Garrison R. F., Hiltner W. A., Schild R. E., 1977, ApJS, 35, 111
Gosset E., Royer P., Rauw G., Manfroid J., Vreux J.-M., 2001, MNRAS, 327, 435
Grevesse N., Asplund M., Sauval A. J., Scott P., 2010, Ap&SS, 328, 179
Grunhut J. H., Wade G. A., 2013, EAS Publ. Ser., 64, 67

Grunhut J. H. et al., 2012, MNRAS, 426, 2208

Hillier D. J., Miller D. L., 1998, ApJ, 496, 407

Howarth I. D., Walborn N. R., Lennon D. J., Puls J., Nazé Y., Annuk K., Antokhin I., Bohlender D., 2007, MNRAS, 381, 433

Hubrig S. et al., 2011, A&A, 528, A151

Hubrig S., Kholtygin A., Scholler M., Langer N., Ilyin I., Oskinova L., 2012, Inf. Bull. Var. Stars, 6019, 1

Hubrig S. et al., 2013, A&A, 551, A33

Kochukhov O., Makaganiuk V., Piskunov N., 2010, A&A, 524, A5

Maíz-Apellániz J., Walborn N. R., Galué H. Á., Wei L. H., 2004, ApJS, 151, 103

Maíz Apellániz J., Sota A., Walborn N. R., Alfaro E. J., Barbá R. H., Morrell N. I., Gamen R. C., Arias J. I., 2011, in Zapatero Osorio M. R., Gorgas J., Maíz Apellániz J., Pardo J. R., Gil de Paz A., eds, Highlights of Spanish Astrophysics VI. Springer-Verlag, Berlin, p. 467

Martins F., Schaerer D., Hillier D. J., 2005, A&A, 436, 1049

Martins F., Donati J.-F., Marcolino W. L. F., Bouret J.-C., Wade G. A., Escolano C., Howarth I. D. Mimes Collaboration, 2010, MNRAS, 407, 1423

Martins F., Marcolino W., Hillier D. J., Donati J.-F., Bouret J.-C., 2014, preprint (arXiv:e-prints)

Meynet G., Maeder A., 2005, A&A, 429, 581

Nazé Y., Ud-Doula A., Spano M., Rauw G., De Becker M., Walborn N. R., 2010, A&A, 520, A59

Petit V., Wade G. A., 2012, MNRAS, 420, 773

Petit V. et al., 2013, MNRAS, 429, 398

Press W. H., Teukolsky S. A., Vetterling W. T., Flannery B. P., 1992, Numerical Recipes in FORTRAN. The Art of Scientific Computing. Cambridge Univ. Press, Cambridge

Schwarzenberg-Czerny A., 1996, ApJ, 460, L107

Sota A., Maíz Apellániz J., Walborn N. R., Alfaro E. J., Barbá R. H., Morrell N. I., Gamen R. C., Arias J. I., 2011, ApJS, 193, 24

Sota A., Maíz Apellániz J., Morrell N. I., Barbá R. H., Walborn N. R., Gamen R. C., Arias J. I., Alfaro E. J., 2014, ApJS, 211, 10

Stellingwerf R. F., 1978, ApJ, 224, 953

Stibbs D. W. N., 1950, MNRAS, 110, 395

Sundqvist J. O., ud-Doula A., Owocki S. P., Townsend R. H. D., Howarth I. D., Wade G. A., 2012, MNRAS, 423, 21

Townsend R. H. D., Owocki S. P., Groote D., 2005, ApJ, 630, L81

ud-Doula A., Owocki S. P., 2002, ApJ, 576, 413

Ud-Doula A., Owocki S. P., Townsend R. H. D., 2008, MNRAS, 385, 97

ud-Doula A., Owocki S. P., Townsend R. H. D., 2009, MNRAS, 392, 1022

ud-Doula A., Sundqvist J. O., Owocki S. P., Petit V., Townsend R. H. D., 2013, MNRAS, 428, 2723

Wade G. A., Landstreet J. D., Elkin V. G., Romanyuk I. I., 1997, MNRAS, 292, 748

Wade G. A., Donati J.-F., Landstreet J. D., Shorlin S. L. S., 2000a, MNRAS, 313, 851

Wade G. A., Kudryavtsev D., Romanyuk I. I., Landstreet J. D., Mathys G., 2000b, A&A, 355, 1080

Wade G. A. et al., 2011, MNRAS, 416, 3160

Wade G. A. et al., 2012a, MNRAS, 419, 2459

Wade G. A. et al., 2012b, MNRAS, 425, 1278

Wade G. A. et al., 2014, in Petit P., Jardine M., Spruit H. C., eds, Proc. IAU Symp. 302, Magnetic Fields throughout Stellar Evolution. Cambridge Univ. Press, Cambridge, p. 265

Walborn N. R., 1972, AJ, 77, 312

Walborn N. R., 1973, AJ, 78, 1067

Walborn N. R., 1980, ApJS, 44, 535

Walborn N. R. et al., 2004, ApJ, 617, L61

Walborn N. R., Sota A., Maíz Apellániz J., Alfaro E. J., Morrell N. I., Barbá R. H., Arias J. I., Gamen R. C., 2010, ApJ, 711, L143

Yusef-Zadeh F., Morris M., White R. L., 1984, ApJ, 278, 186

[1]*Department of Physics, Royal Military College of Canada, PO Box 17000 Station Forces, Kingston, ON K7K 7B4, Canada*

[2]*Departamento de Física, Universidad de La Serena, Av. Cisternas 1200 Norte, La Serena, Chile*

[3]*European Southern Observatories, Karl-Schwarzschild-Str. 2, D-85748 Garching, Germany*

[4]*LUPM-UMR5299, CNRS & Université Montpellier II, Place Eugène Bataillon, F-34095 Montpellier, France*

[5]*Department of Physics and Astronomy, Bartol Research Institute, University of Delaware, Newark, DE 19716, USA*

[6]*Institut für Astronomie und Astrophysik der Universität München, Scheinerstr. 1, D-81679 München, Germany*

[7]*Department of Astronomy, University of Wisconsin-Madison, 475 N Charter Street, Madison, WI 53706, USA*

[8]*Space Telescope Science Institute, 3700 San Martin Drive, Baltimore, MD 21218, USA*

[9]*UJF-Grenoble 1/CNRS-INSU, Institut de Planétologie et d'Astrophysique de Grenoble (IPAG) UMR 5274, F-38041 Grenoble, France*

[10]*Instituto de Astrofísica de Andalucía-CSIC, Glorieta de la Astronomía s/n, E-18008 Granada, Spain*

[11]*Instituto de Astrofísica de La Plata (CCT La Plata-CONICET, Universidad Nacional de La Plata), Paseo del Bosque s/n, 1900 La Plata, Argentina*

[12]*Las Campanas Observatory, Observatories of the Carnegie Institution of Washington, La Serena, Chile*

[13]*Research Associate FRS-FNRS, Département AGO, Université de Liège, Allée du 6 Août 17, Bat. B5C, B-4000 Liège, Belgium*

[14]*Groupe d'Astrophysique des Hautes Energies, Institut d'Astrophysique et de Géophysique, Université de Liège, 17, Allée du 6 Août, B5c, B-4000 Liège, Belgium*

[15]*Penn State Worthington Scranton, Dunmore, PA 18512, USA*

This paper has been typeset from a TEX/LATEX file prepared by the author.